Core transport barriers induced by fast ions in global gyrokinetic GENE simulations

A. Di Siena,[1] R. Bilato,[2] T. Görler,[2] E. Poli,[2] A. Bañón Navarro,[2] D. Jarema,[2] and F. Jenko[2]

[1] *The University of Texas at Austin 201 E 24th St 78712 Austin Texas USA*

[2] *Max Planck Institute for Plasma Physics Boltzmannstr 2 85748 Garching Germany*

A novel type of internal transport barrier (ITB) called F-ATB (fast ion-induced anomalous transport barrier) has been recently observed in state-of-the-art global gyrokinetic simulations on a properly optimized ASDEX Upgrade experiment and presented in A. Di Siena et al. Phys. Rev. Lett. **127** 025002 (2021). Unlike the transport barriers previously reported in the literature, the trigger mechanism for the F-ATB has been shown to be a wave-particle resonant interaction between supra-thermal particles - generated via ion cyclotron resonance heating (ICRH) - and ion scale plasma turbulence. This resonant mechanism strongly depends on the particular shape of the fast ion temperature and density profiles. Therefore, to further improve our theoretical understanding of this transport barrier, we present results exploring the parameter space and physical conditions for the F-ATB generation by performing a systematic study with global GENE simulations. Particular emphasis is given to the transport barrier width and its localization by scanning over different energetic particle temperature profiles. The latter are varied in amplitude, half-width, and radial localization of an ad-hoc Gaussian-like energetic particle logarithmic temperature gradient profile. For the reference parameters at hand, a threshold in the ratio between the fast ion and electron temperature and the amplitude of the fast ion logarithmic temperature gradient is identified to trigger the transport barrier effectively. The role of $q = 1$ rational surface to the transport barrier formation is investigated as well by retaining electromagnetic effects and its impact found to be negligible for this particular barrier formation mechanism.

I. INTRODUCTION

One of the primary goals of fusion research is identifying possible experimental actuators to control turbulent transport in magnetic confinement devices. This is particularly important in view of future fusion reactors to maximize the fusion triple product by increasing the on-axis plasma pressure and hence the fusion output. Promising results along these lines are related to the formation of narrow regions in the core of fusion devices with reduced turbulent transport, commonly called internal transport barriers (ITBs) [1] (and reference therein). Internal transport barriers have been widely observed in magnetic confinement devices under different experimental conditions in both tokamaks and stellarators [2–14]. Their formation is typically associated with nearly flat or reversed shear configurations $s = \rho/q \ (dq/d\rho) < 0$ (with q safety factor and ρ the radial coordinate) [15–17], gaps between rational surfaces and violation of interaction between MHD modes located on the neighboring surfaces [18, 19] and fast ion effects in highly electromagnetic regimes [20, 21].

While a large variety of ITBs has been reported in the literature from experimental studies, only a limited number of transport barriers has been observed with global gyrokinetic codes up-to-date, e.g., Refs. [22, 23] for reduced adiabatic electron setups. Recently, a new type of internal transport barrier has been first predicted and then observed via global gyrokinetic GENE [24, 25] simulations on a properly designed ASDEX Upgrade discharge, revealing signatures of improved plasma confinement consistently with the numerical results [26]. As shown in Ref. [26] by state-of-the-art GENE simulations (including kinetic electrons with realistic mass ratio, supra-thermal particles modeled with realistic distributions, electromagnetic effects and collisions), this transport barrier, called F-ATB (fast ion-induced anomalous transport barrier), leads to a full turbulence suppression within its radial domain and an increase in the neoclassical counterpart. The trigger mechanism responsible for its generation is the wave-particle resonance interaction between ion-scale plasma turbulence and supra-thermal particles generated via ion cyclotron resonance heating (ICRH), recently identified in both tokamak and stellarator devices [27–29]. These findings hence suggest an intriguing possibility to access fusion relevant physical conditions more easily.

According to analytic theory and gyrokinetic results, ion-temperature-gradient (ITG) micro-instabilities can interact with certain plasma species whenever their magnetic drift frequency (ω_{df}) is comparable with the ITG frequencies (ω_{ITG}) for some relevant wave-numbers. Whilst this condition is hardly matched by thermal species (typically having $\omega_{ITG} \gg \omega_{df}$), it is well fulfilled by mildly supra-thermal particles, commonly generated via auxiliary heating schemes in nowadays experiments, e.g. neutral-beam-injection (NBI) and ICRH. Such fast particles (called "supra-thermal" and/or "energetic/fast" ions in this manuscript) have energy typically smaller than the critical energy (energetic particle slowing down on thermal ions equals that on thermal electrons). Given the nature of this resonant interaction - involving a magnetic drift resonance -, it occurs over a large number of precession-bounce resonances.

As discussed in detail in Ref. [27], an additional constraint on the fast particle logarithmic gradients has to be fulfilled to achieve an effective ITG stabilization via this wave-particle interaction. More specifically, the fast

ion logarithmic temperature gradient has to largely overcome the corresponding density gradient to allow an effective energy transfer from the ITGs to the fast particles, thus making this wave-particle resonant effect accessible mainly for ICRH schemes. Further details can be found in Refs. [27, 28]. Signatures of this beneficial fast ion effect on turbulent transport have been observed at ASDEX Upgrade [26], JET [30] and are also expected for W7-X [29] and during the ramp-up phase of an ITER standard scenario [27].

Given the high relevance of this wave-particle resonant interaction in (possibly) improving plasma confinement by triggering this novel type of transport barriers, this contribution explores the parameter space and physical conditions for the F-ATB formation by performing a systematic study with global GENE simulations. Each of the GENE simulations required approximately 0.8 million CPUh on the Marconi Skylake partition. Particular attention is given to analyze the transport barrier width and its localization by scanning over different energetic particle temperature profiles. The physics inputs are derived from the reference ASDEX Upgrade discharge #36637 at $t = 4.1s$ which showed an improvement in the plasma performances. State-of-the-art global electromagnetic gyrokinetic GENE simulations have been performed on this specific discharge in Ref. [26] analyzing the F-ATB and the nature of its trigger mechanism.

It is important to mention here, that radially-global gyrokinetic simulations are essential to fully capture the transport barrier properties, such as global $E \times B_0$ flows, their effect on turbulent transport and the dynamics of turbulent avalanches in the proximity of the transport barrier. Whilst flux-tube linear and nonlinear simulations can locate with good approximation the center of the F-ATB, they fail in fully capturing the transport barrier width and the turbulent levels at the radial boundaries of the transport barrier [26].

The remainder of this paper is organized as follows. Section II briefly presents the code GENE and the numerical setup used for carrying out the simulations discussed throughout this paper. The physical parameters, plasma profiles and geometry - inspired from the ASDEX Upgrade discharge #36637 at $t = 4.1s$, previously studied in Ref. [26] - are discussed in Section III, together with the analytic Gaussian-like approximation used for modeling the energetic particle logarithmic temperature gradient profile. The latter defines different fast particle temperatures that vary one to the other in the amplitude, half-width, and radial localization of the Gaussian-like energetic particle logarithmic temperature gradient profile. The impact of each of these different parameters on the F-ATB properties is studied in details in Sec. IV-VII. In Sec. VIII the role of the $q = 1$ rational surface on the F-ATB formation is investigated via global electromagnetic simulations. Conclusions are drawn in Sec. IX, while convergence studies are provided in the appendix A.

II. NUMERICAL MODEL AND SETUP

A. Model description

The numerical simulations presented in this paper have been performed with the Eulerian gyrokinetic code GENE [24, 25]. GENE solves the coupled Vlasov-Maxwell system of equations on the field-aligned coordinate grid (x, y, z) in configuration space and $(v_\parallel, \mu)$ in velocity. Here, $x = \rho_{tor}a = \sqrt{\Phi_{tor}/\pi B_0}$ denotes the radial coordinate, with Φ_{tor} toroidal flux, a the minor radius and B_0 the on-axis magnetic field; $y = x_0 (q\chi - \varphi)/q(x_0)$ the bi-normal direction with x_0 the center of the radial domain, χ the straight-field-line poloidal angle, φ the toroidal angle and q the safety factor; and z the distance along a field line. Moreover, $v_\parallel$ represents the velocity component parallel to the background magnetic field B_0 and μ the magnetic moment. While fixed equidistant grids are used for the radial (x), parallel field (z) and $v_\parallel$ directions, the magnetic moment (μ) is discretized with Gauss-Laguerre integration points. The bi-normal direction (y) is represented in Fourier space. The underlying gyrokinetic equations are solved in GENE for the perturbed part of distribution function f_1 assuming a stationary background distribution f_0 (so called δf approach). Whilst different choices of f_0 (both analytic and numerical) are currently supported in GENE [31–33], an equivalent Maxwellian distribution function is employed throughout this paper for simplicity unless stated otherwise. The level of approximation in modeling supra-thermal particle distributions with a Maxwellian background instead of more realistic distribution functions will be discussed in Section IV. Kinetic electrons with realistic ion-to-electron mass ratio, collisions modeled with a linearized Landau operator with energy and momentum conserving terms [34] and a realistic magnetic geometry are retained for the present study. To keep the numerical cost of the simulations at a reasonable level, electromagnetic fluctuations are neglected unless stated otherwise. This approximation is not expected to alter qualitatively the global structure of the F-ATB [26].

In radially global simulations, GENE allows the use of block-structured grids, e.g., radially dependent velocity grids that are properly optimized (based on the temperature profile of a selected plasma species) to reduce the resolution requirements in the velocity space without losing in accuracy [35]. This specific feature is of critical importance for the numerical simulations presented in this paper, otherwise requiring a prohibitive velocity space resolution to capture the extreme changes in the energetic particle temperature profiles. Although GENE can be run either in a single flux-tube (radially-local) or a broad radial domain (radially-global), only the latter version of the code is used for the nonlinear simulations in the present work. This is particularly important to retain global effects correctly, such as turbulence avalanches, turbulence spreading and radially-global zonal flow structures, which are important in the present study to de-

scribe the global features of the F-ATB.

There are two distinct ways of running GENE in radially global simulations, the so-called flux-driven and gradient-driven setups. The flux-driven approach consists in employing particle and energy sources which mimic the external sources applied in experiments and allow the pressure profile to freely adjust until reaching a steady-state solution. Whilst Neumann boundary conditions are employed in the inner boundary, Dirichet boundary conditions are used on the outer boundary. Dirichlet boundary conditions require radial buffer regions (typically few percent of the whole radial domain) to smoothly damp the fluctuation levels at the radial boundary. The steady-state solution is reached when the turbulent fluxes match the volume integral of the external sources in the simulated radial domain. This condition is typically achieved when running the turbulence simulations up to the confinement time-scale (several order of magnitude larger than the turbulence time-scale), making flux-driven simulations extremely demanding numerically. The gradient-driven approach, on the other hand, consists in applying a Krook-type operator to maintain the averaged profiles of each species fixed to the initial ones. Dirichlet boundary conditions are applied for both inner and outer radial boundaries. The main advantage of running in gradient-driven mode is that the turbulence simulation does not need to be run up to the confinement time scale but only on the turbulence time scale, thus significantly reducing the numerical cost of each simulations. Further details on the different numerical schemes and implementation of flux-driven and gradient-driven setups can be found in Ref. [36].

B.   Numerical setup and resolution

In the following, the main parameters and resolutions employed throughout this work are summarized. The numerical simulations are performed (unless stated otherwise) in the radial domain $\rho_{tor} = [0.05 - 0.55]$. The grid resolution employed in the radial (x), bi-normal (y) and field-aligned (z) directions is respectively ($nx0 \times nky0 \times nz0$) = ($256 \times 48 \times 32$). The discretized toroidal mode number is given by $n = n_{0,min} \cdot j$ with j being integer-valued in the range $j = [0, 1, 2, ..., nky0 - 1]$ and $n_{0,min} = 2$.

As previously mentioned, a radially dependent block-structured grid is found to be essential to reduce the velocity resolution requirements needed to capture the sharp changes in the fast ion temperature profile. In the present paper, we employed a velocity grid divided into five different blocks. It has been properly designed to resolve correctly the ($v_{\parallel}, \mu$)-dynamics for each different plasma species with 48 points along the parallel velocity and 24 along the magnetic moment. This block-structured grid is shown in Fig. 1a in the ($v_{\parallel}, \mu, \rho_{tor}$)-space, in Fig. 1b for its slice at $\mu = 0$ and in Fig. 1c at the plane at $v_{\parallel} = 0$. Dedicated convergence studies on
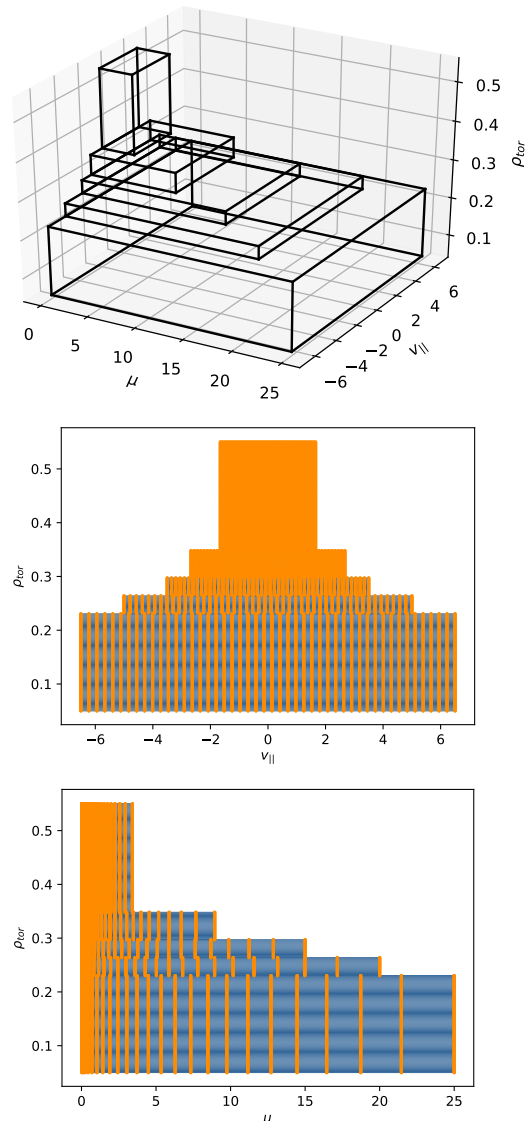

FIG. 1. Reference block-structured grid with five blocks in a) ($\rho_{tor}, v_{\parallel}, \mu$) used throughout this paper (unless stated otherwise) and its slices in b) ($\rho_{tor}, v_{\parallel}$) and c) ($\rho_{tor}, \mu$). The vertical orange lines in each blocks of b) and c) represent the ($v_{\parallel}, \mu$) grid points used in each directions.

the specify structure of the velocity space grid are shown in the Appendix A. All the numerical simulations presented within this paper have been performed running GENE in gradient-driven mode. Therefore, Krook-type particle and heat operators have been applied to keep the plasma profiles (on average) fixed to the initial ones. The amplitude of the Krook heat (γ_k) and particle (γ_p) coefficients used are, respectively, $\gamma_k = 0.085 c_s/a$ and $\gamma_p = 0.85 c_s/a$. Here, $c_s = (T_e/m_i)^{1/2}$ represents the sound speed, with T_e the electron temperature at the reference radial position and m_i the bulk ion mass in proton units.

Buffer regions covering 10% of the main simulation radial domain have been employed in this study near the domain boundaries to ensure consistency with the Dirichlet boundary conditions. In these buffer areas an artificial Krook damping operator γ_b is applied with an amplitude $\gamma_b = 1.0 c_s/a$. Finally, to reduce the otherwise prohibitive computational cost of these simulations, numerical fourth order hyperdiffusion is used to damp fluctuations at large toroidal mode number due to electron temperature gradient (ETG) modes.

III. PHYSICAL CONDITIONS FOR TRANSPORT BARRIER FORMATION

The parameter space and physical conditions possibly leading to the F-ATB generation are here explored by performing a series of (gradient-driven) global gyrokinetic GENE simulations inspired by the reference AS-DEX Upgrade discharge #36637 [37]. A detailed description of this discharge can be found in Ref. [26]. Nevertheless, we briefly summarize here the main discharge parameters. This is an H-mode deuterium plasma heated with constant $P = 2.5$MW electron-cyclotron-resonance-heating (ECRH) and $P = 2.5$MW neutral-beam-injected (NBI) - source 8 at 93.5keV. Moreover, a ramp-up of the ion-cyclotron-resonance-heating (ICRH) power is performed going from 0 to 3.5MW. The ICRH frequency is 36.5MHz and the antenna is operating in dipole phasing. For this study we focus our analyses on the time slice $t = 4.1$s, namely when the maximum ICRH power is applied ($P = 3.5$MW). This phase corresponds to the physical conditions where the ion temperature profile reaches the maximum value on-axis with no degradation of the plasma confinement (despite the increase in the auxiliary ICRH heating power). The time traces of the heating power, confinement time and snapshots of the ion temperatures at different time-slices can be found in Ref. [26]. Ref. [26] presented compelling numerical evidence - based on radially global electromagnetic GENE simulations - showing a novel type of transport barrier in the GENE simulations. The magnetic equilibrium is shown in Fig. 2a-b together with the safety factor profile. It has been reconstructed by CLISTE [38] and read into GENE via numerical field line tracing provided by the TRACER-EFIT interface [39]. As shown in Fig. 2b, CLISTE predicts a monotonic safety factor profile always above $q = 1$. The role of the rational surface at $q = 1$ and negative shear configurations on the F-ATB properties are investigated in Sec. VIII.

The thermal ion and electron temperature profiles are illustrated in Fig. 2c while the thermal ion, electron and ICRH-hydrogen minority density profiles in Fig. 2d. While the main ion temperature profile has been obtained from IDI [40], the electron temperature and density profiles from IDA [41]. The logarithmic density gradient ($\omega_{n,h} = -(1/n_h)\, \mathrm{d}n_h/\mathrm{d}\rho_{tor}$) of the ICRH-hydrogen minority is shown in Fig. 2e. This quantity is particu-

larly important in the dynamics of the resonant interaction between supra-thermal particles and ITGs, since an effective turbulence stabilization requires $\omega_{T,h} \gg \omega_{n,h}$ [27, 28]. Here, $\omega_{T,h} = -(1/T_h)\, \mathrm{d}T_h/\mathrm{d}\rho_{tor}$ represents the energetic particle (hydrogen minority) logarithmic temperature gradient. Throughout this paper $\omega_{n,h}$ is kept fixed to the nominal profile of Fig. 2e.

In the present paper, we investigate the F-ATB properties for different shapes of the energetic particle profiles. As demonstrated in details in Refs. [27, 28] via analytic theory and numerical simulations, changes in the fast ion temperatures strongly affects the wave-particle resonant dynamics via modifications on the energetic particle magnetic-drift frequency. Therefore, a combination of ten different fast particle temperature profiles has been selected for these analyses. To simplify the definition of the energetic particle temperature profiles, an analytic expression is used

$$T_h = T_{h,0} \cdot \exp(-\omega_{T_{h,0}} \cdot \delta_x \cdot \tanh((\rho_{tor} - \rho_0)/\delta_x)). \quad (1)$$

Eq. 1 leads to the Gaussian-like function for the logarithmic temperature gradients of the supra-thermal particle species,

$$\omega_{T,h} = -(1/T_h)dT_h/d\rho_{tor} = \omega_{T_{h,0}} \cdot \mathrm{sech}^2((\rho_{tor} - \rho_0)/\delta_x). \quad (2)$$

Here, $T_{h,0} = 8.3$keV is a dimensional factor giving units to T_h. The three different free parameters of Eqs. 1, 2 are ρ_0, δ_x and $\omega_{T_{h,0}}$. They represent, respectively, the position (in ρ_{tor}) of the peak of the fast ions logarithmic temperature gradient, the full width at half maximum of the Gaussian-like function and its amplitude. Throughout this paper, the impact of each of these different parameters on the F-ATB properties is investigated in details.

It is worth mentioning here that the reference profile used in the following studies (called profile A) is constructed to approximate the realistic ICRH-hydrogen minority profile computed by TORIC/SSFPQL [42, 43] for the reference AUG discharge #36637 at $t = 4.1$s. A comparison of the realistic fast ion temperature profile and its logarithmic gradient (used in Ref. [26]) with their simplified expression constructed by Eqs. 1, 2 is illustrated in Fig. 3.

To evaluate how the specific shapes of the energetic particle temperature profiles affect the F-ATB properties, we present below a baseline scenario obtained by neglecting the fast hydrogen minority in the GENE simulations. These reference results will be employed in the following Sections to estimate the most effective fast particle temperature profiles maximizing the turbulence suppression via the wave-particle resonant interaction, namely the profiles leading to the strongest turbulence suppression in comparison with the case without fast particles. When neglecting the supra-thermal particles, the time-averaged (over the nonlinear saturated phase) heat flux profiles reach large amplitudes, as shown in Fig. 4. These simulations have been obtained by enforcing quasi-neutrality on the thermal ion density profile and setting it equal
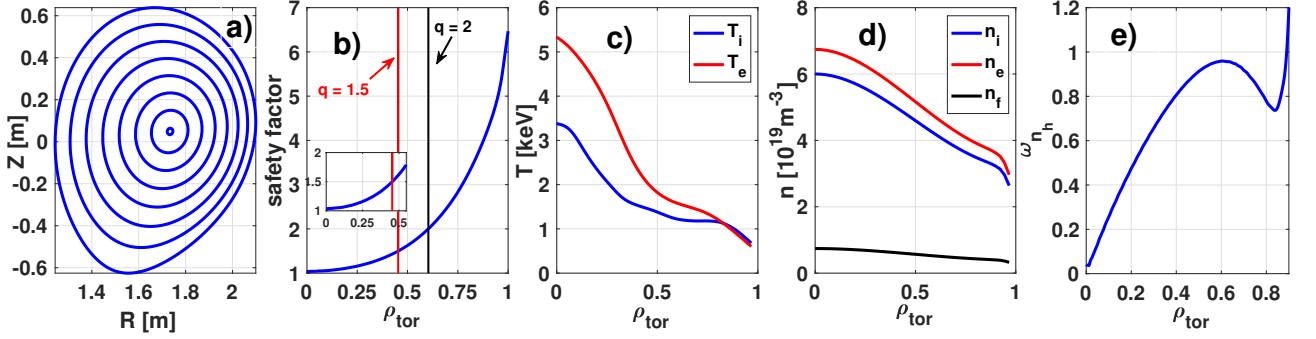
FIG. 2. a) Contours of constant poloidal flux of magnetic equilibrium reconstructed by CLISTE, b) safety factor profile, c) bulk ion and electron temperature profiles, d) corresponding density profiles of bulk ion, electron and hydrogen minority and e) logarithmic density gradient of the hydrogen minority in ASDEX Upgrade discharge #36637 at $t = 4.1s$ used as input to GENE. The positions of the rational surfaces $q = 1.5$ and $q = 2$ are marked, respectively, by the red and black vertical lines. The inlays in b) contains a zoom into the safety factor profile in $\rho_{tor} = [0 - 0.55]$.
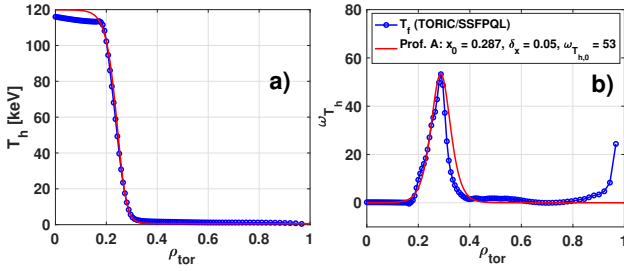
FIG. 3. Radial profile of the hydrogen minority a) temperature and b) logarithmic temperature gradient. The blue line in each plots denotes the temeprature profile computed by TORIC/SSFPQL for the ASDEX Upgrade discharge #36637 at $t = 4.1s$, whilst the red line its simplified analytic approximation.
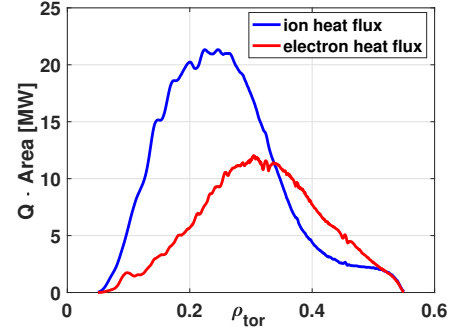

FIG. 4. Radial profile of the heat flux of the bulk ions and electrons obtained from GENE averaged over the time domain $t[c_s/a] = [400 - 600]$. The supra-thermal particle species are neglected.

to the electron one. The magnetic geometry is set equal to the experimental one retaining the effect of fast ions. The heat flux (Q) of the generic species s is computed as

$$Q_s = \langle \mathbf{Q_s} \cdot \nabla x \rangle_S = \langle \int \frac{1}{2} m_s v^2 \delta f_{1,s} \left(\mathbf{v_{E \times B}} \cdot \nabla x \right) d^3 v \rangle_S. \tag{3}$$

Here, m_s and $\delta f_{1,s}$ represent, respectively, the mass and the perturbed part of the distribution function of the species s ($s = i, e, h$ stand respectively for thermal ions, electrons and fast hydrogen minority), while $\mathbf{v_{E \times B}}$ the $\mathbf{E} \times \mathbf{B}$ velocity and $\langle \cdot \rangle_S$ the surface average.

IV. IMPACT OF THE AMPLITUDE OF THE LOGARITHMIC FAST ION TEMPERATURE GRADIENT

We begin by studying the effect that $\omega_{T_h,0}$ has on the F-ATB. This parameter defines the amplitude of the Gaussian-like logarithmic temperature gradient and thus

determines the on-axis value of T_h. To cover a broad range of energetic particle profiles (and hence external heating powers), we have selected four different cases (labelled prof. A to D). They are constructed from Eq. 1 by keeping $\delta_x = 0.05$, $\rho_0 = 0.287$ and varying the value of $\omega_{T_h,0}$ from $\omega_{T_h,0} = 30$ to $\omega_{T_h,0} = 53$ (nominal value). The resulting fast particle temperature profiles and their logarithmic gradients are illustrated, respectively, in Fig. 5a and Fig. 5b. With the numerical setup summarized in Section II, we performed global GENE simulations for each of the distinct fast ion profiles shown in Fig. 5. The magnetic geometry and background profiles are fixed to the reference ones of Fig. 2.

The radial profiles of the time-averaged turbulent fluxes obtained from the simulations corresponding to the different energetic particle profiles are shown in Fig. 6 for each plasma species. Furthermore, the overall (ion + electron + energetic particle) turbulent heat flux profile evolution is illustrated in Fig. 7 for the reference fast ion temperature prof. A and prof. D. A first observation is
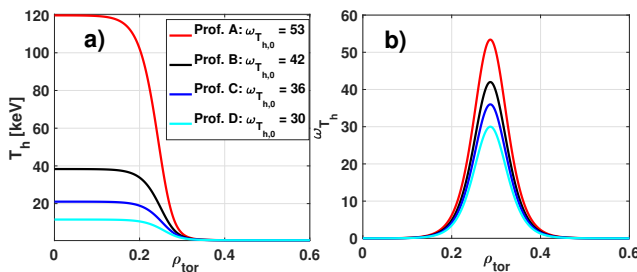
FIG. 5. Radial profiles of the hydrogen minority a) temperature and b) logarithmic temperature gradient corresponding to four different values of $\omega_{T_{h,0}}$.

that the transport barrier - localized in the radial domain $\rho_{tor} = [0.2 - 0.3]$ for the reference fast particle profile (prof. A) - disappears as $\omega_{T_{h,0}}$ is reduced below the critical value $\omega_{T_{0,c}} = 42$. Without the transport barrier the overall turbulent flux profile approaches the one obtained in the absence of supra-thermal particles (see Fig. 6d), revealing a progressive turbulence destabilization within the radial region of the F-ATB as $\omega_{T_{h,0}}$ is reduced.

The energetic particle heat flux profile undergoes significant variations (see Fig. 6c) for $\rho_{tor} < 0.3$, where the fast ion heat flux is reduced from 20MW (prof. D) to roughly 0MW (prof. A) at $\rho_{tor} = 0.25$, suggesting a gradual enhancement of the beneficial fast ion effect on ITGs as T_h/T_e increases with $\omega_{T_{h,0}}$. To investigate the specific role played by the simultaneous changes in the energetic particle temperature and its gradient on the underlying ITGs, linear flux-tube scans are performed at the reference position $\rho_{tor} = 0.25$ (center of the F-ATB). The results are illustrated in Fig. 8b for the toroidal-mode number $n = 21$, corresponding to the most unstable mode at the position of interest. No qualitative differences are observed if the toroidal-mode number is changed. At fixed logarithmic fast ion temperature gradients (above $\omega_{T_h} = 10$), the characteristic "sweet-spot" in the ratio T_h/T_e is observed (blue region in Fig. 8b). It denotes the optimal fast ion temperature locating the phase-space resonance into the minimum negative drive term for the supra-thermal particles (namely $\partial_x f_0$ with x the radial direction). These results are consistent with the theoretical predictions of Refs. [27, 28]. In particular, we note that when T_h/T_e decreases, the wave-particle resonant layers move to larger $(v_\parallel, \mu)$-velocities resulting in a linear micro-instability de-stabilization when they are located into the positive fast ion drive regions ($v_\parallel^2 - \mu B_0 > 3/2$). The readers are referred to Refs. [27, 28] for a detailed description of the specific interplay between stabilizing and de-stabilizing wave-particle resonant interactions. The energetic particle logarithmic temperature gradient effectively enhances the fast ion effects on the underlying ITGs. The operational points for the ratio T_h/T_e and the fast ion logarithmic temperature gradient of the four different profiles studied in this Section are marked in Fig. 8b and the T_h/T_e profiles are shown in Fig. 8a. It

is clear that only prof. A and B have fast ion temperatures exceeding the minimum value of $T_h/T_e = 4$ to effectively stabilize ITG micro-instabilities (delimited by the two white vertical lines), whilst prof. C and D lead to a linear growth rate destabilization. These findings are consistent with the nonlinear results of Fig. 6.

The mild differences in the energetic particle heat flux profiles observed in Fig. 6c for $\rho_{tor} > 0.3$ are related to the negligible variations in the ratio T_h/T_e over the four fast ions profiles employed throughout this Section.

At the narrow radial layer where the wave-particle resonant interaction turns from stabilizing to destabilizing (i.e., $\rho_{tor} = 0.3$), a large fast ion heat flux is observed for each fast ion temperature profile. At this position, the destabilizing fast ion resonant effect on micro-turbulence is amplified by their large logarithmic temperature gradient. However, this is also the radial domain where electromagnetic fast ion effects [44–46] are more pronounced possibly due to the large fast ion pressure gradient. To estimate the role of finite-β_e on the turbulent fluxes of each plasma species, we perform, in the remaining part of this Section, global GENE simulations retaining electromagnetic fluctuations with $\beta_e(\rho_{tor} = 0.3) = 8\pi T_e n_e/B_0^2 = 0.4\%$ for the case labeled prof. A. The results are shown in Fig. 9. The electrostatic and electromagnetic GENE results of Fig. 9 identified by the black and blue lines have been obtained by modeling the energetic particle equilibrium distribution function with a bi-Maxwellian. The parallel and perpendicular temperature profiles have been set equal to the ones computed by TORIC/SSFPQL for the experimental case summarized in Ref. [26]. Consistently with Ref. [44–46], electromagnetic effects reduce turbulent transport for each plasma species, in particular for the fast ions, which give the largest contribution at that position. This turbulence suppression is largely localized in the radial domain $\rho_{tor} = [0.3-0.4]$ and leads to a significant stabilization of the fast ion heat flux, which is reduced by $\sim 60\%$ (from roughly 18MW to 7MW) at $\rho_{tor} = 0.3$. No linearly unstable Alfvénic fast-ion driven modes are observed. These results might be a hint to a nonlinear wave-wave interplay between marginally stable fast ion modes and turbulence, proposed in Ref. [45, 46] to explain the numerical gyrokinetic simulations and experiments. A more detailed analysis assessing the role of Alfvén modes (stable, marginally stable or unstable) on the F-ATB is left for future studies.

To assess the relevance of correctly capturing the temperature anisotropies arising from the ICRH scheme, we add in Fig. 9 the time-averaged (over the nonlinear saturated phase) heat flux profiles carried by the different species in the electrostatic limit by using a Maxwellian background for the supra-thermal species. By looking at the electrostatic results of Fig 9, only minor differences are observed for the thermal species (bulk ions and electrons). However, we note a reduction in the supra-thermal ion heat flux at $\rho_{tor} = 0.3$, which diminishes by $\sim 30\%$ (from roughly 18MW to 13MW) when the Maxwellian fast-ion distribution is replaced by
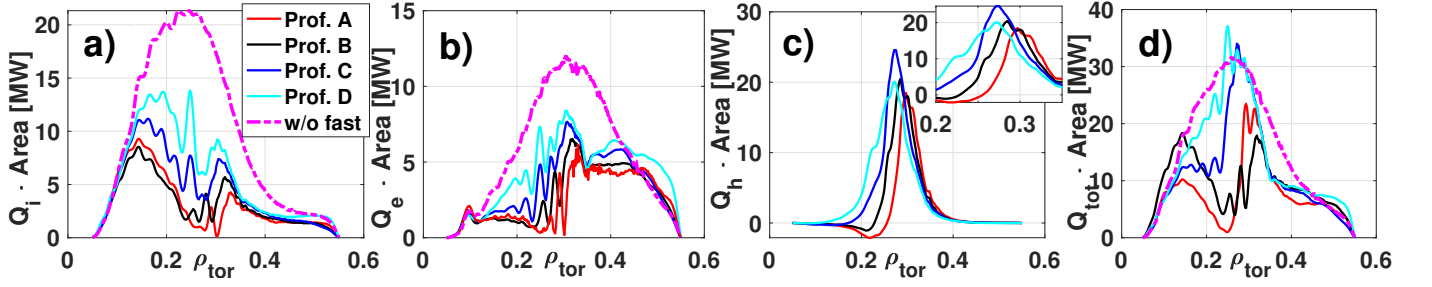
FIG. 6. Radial profile of the a) bulk ions, b) electrons, c) hydrogen minority species and d) overall (thermal ion + electron + fast hydrogen) heat fluxes averaged over the time domain $t[c_s/a] = [400 - 600]$ corresponding to the four different fast ion profiles of Fig. 5. The inlay in c) contains a zoom into the energetic particle fluxes in $\rho_{tor} = [0.2 - 0.35]$. The turbulent fluxes obtained by neglecting the energetic particles (Fig. 4) are shown in magenta as reference.
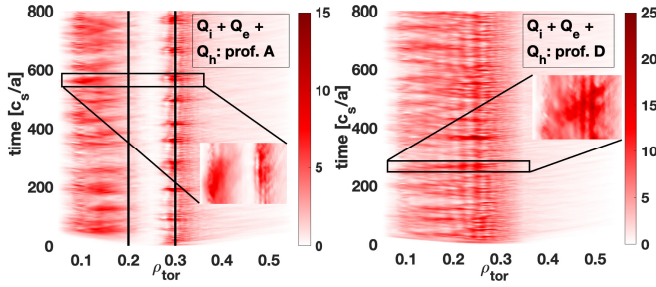

FIG. 7. Time evolution of the radial profile of the total heat flux (thermal ions + electrons + hydrogen) in MW corresponding to the cases labelled a) prof. A and b) prof. D. The vertical black lines in a) delimit the boundary positions of the transport barrier. Their radial coordinates have been computed as the position where the overall time-averaged (thermal ions + electrons + hydrogen) fluxes (see Fig. 6d) reach half-value before and after the transport barrier (i.e., $\rho_{tor} = [0.1 - 0.25]$ (left black line) and $\rho_{tor} = [0.3 - 0.4]$ (right black line)).
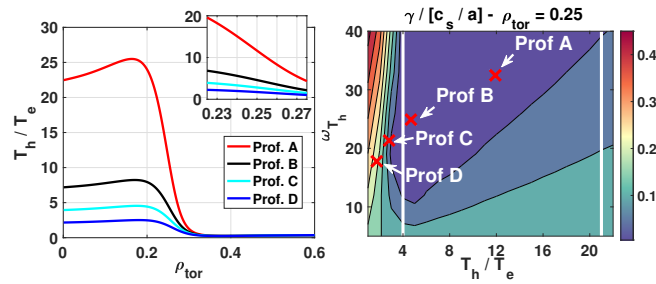

FIG. 8. a) Radial profile of the fast ion to electron temperature ratio T_h/T_e for the four different energetic particle temperature profiles of Fig. 5; and b) contour plot of the most unstable linear growth rate at the toroidal mode number $n = 21$ at $\rho_{tor} = 0.25$ for different T_h/T_e and ω_{T_h}. The reference points corresponding to the values of $(T_h/T_e, \omega_{T_h})$ for the fast ion profiles labelled prof. A to D are highlighted with red crosses.

a bi-Maxwellian. Interestingly, the outward fast ion flux shrinks in the radial direction. This is likely to be connected with the different parallel and perpendicular logarithmic fast particle temperature gradients, which modify the fast ion drive term, thus indirectly affecting the phase-space localization of the resonance layers. Preliminary results assessing the role of the fast ion temperature anisotropies on the wave-particle resonant interaction can be found in Refs. [47].

V. IMPACT OF THE HALF-WIDTH OF THE LOGARITHMIC FAST ION TEMPERATURE GRADIENT

The second parameter defining the radial profile of supra-thermal particle species is δ_x. It represents the half-width of the Gaussian-like logarithmic temperature gradient and, similarly to $\omega_{T_h,0}$, determines also the on-axis fast ion temperature. Throughout this Section, the turbulent fluxes of the reference prof. A ($\delta_x = 0.05$) are compared with those obtained by reducing (prof. E, i.e. $\delta_x = 0.04$) and increasing (prof. F, i.e., $\delta_x = 0.055$) the half-width of the fast ion temperature gradients. The energetic particles profiles are illustrated in Fig. 10. Larger values of δ_x have not been explored in this work, since the resulting fast particle temperature profiles will set more demanding constraints over the radial dependent block-structured grids to fully resolve the velocity directions for each plasma species. The radial profiles of the turbulent fluxes carried by each plasma species are illustrated in Fig. 11. While no significant variations are observed in the electron heat fluxes in the whole radial region of interest, minor - but still relevant - changes are found for the bulk and supra-thermal ion heat fluxes within the transport barrier. More precisely, a reduced ion-scale turbulence stabilization is observed for the case labelled prof. E when compared to the results obtained with the other profiles at $\rho_{tor} = 0.25$ (see Fig. 11a)). This result is consistent with a corresponding weakening of the wave-particle resonant interaction within the F-ATB. In particular, the region of inward fast ion heat flux - corre-
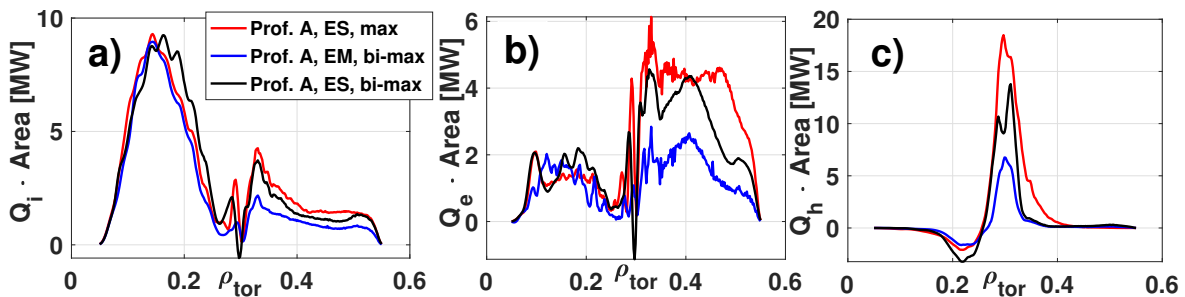
FIG. 9. Radial profile of the heat flux of a) bulk ions, b) electrons and c) hydrogen minority species - averaged over the time domain $t[c_s/a] = [400 - 600]$ - corresponding to the fast particle profile labelled prof. A and different fast background distribution functions. While a Maxwellian is employed for the red line, a bi-Maxwellian background is used for the black and blue lines. Electromagnetic fluctuations are considered only for the blue line.
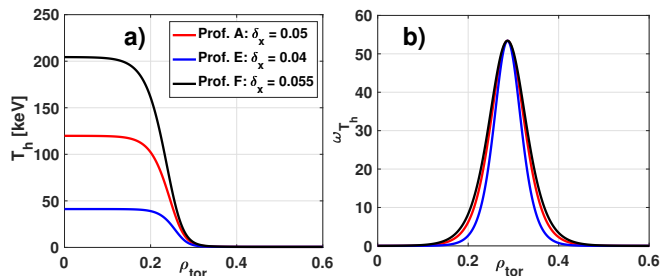

FIG. 10. Radial profiles of the hydrogen minority a) temperature and b) logarithmic temperature gradient corresponding to three different values of δ_x.

sponding to the radial domain where the resonant interaction is most effective - is reduced in both amplitude (by roughly 66%) and radial extent (from $\rho_{tor} = [0.15 - 0.25]$ to $\rho_{tor} = [0.18 - 0.23]$) for the case labelled prof. E (see Fig. 11c)), thus decreasing the beneficial supra-thermal ion effects on turbulent transport. This leads to more localized transport barriers, as shown in Fig. 12, which illustrates the time evolution of the overall radial profile of the turbulent heat fluxes. Therefore, despite the minor variations in the thermal ion and supra-thermal hydrogen fluxes, non-negligible effects on the transport barrier width are observed. These findings are consistent with the linear flux-tube results of Fig. 13b showing the growth rate dependence of the toroidal-mode number $n = 21$ with the T_h/T_e and the fast ion logarithmic temperature gradient at the position $\rho_{tor} = 0.27$. The corresponding T_h/T_e for each profiles are illustrated in Fig. 13a. No qualitative differences are observed if the toroidal-mode number is changed. Fig. 13b reveals that whilst the ratio T_h/T_e is large enough for prof. A and prof. F to reach the optimal temperatures to stabilize ITG micro-instabilities, this does not happen for prof. E, for which the resonant layers still lie in the destabilizing phase-space region of the energetic particle drive, namely at $T_h/T_e < 4$. Therefore, at $\rho_{tor} = 0.27$, the combination of fast ion temperature and temperature gradients

for prof. E leads to a linear ITG destabilization, thus reducing the radial extent of the transport barrier, consistently with Fig. 11d and Fig. 12. These results show that - for a fixed value of $\omega_{T_{h,0}}$ (amplitude of the logarithmic fast ion temperature gradient) - broader energetic particle temperature gradient profiles can trigger transport barriers more effectively. It is worth mentioning here that the supra-thermal particle temperature and its gradients are however limited by the onset of electromagnetic fast particle-driven turbulence [48] which is well-known to be detrimental for plasma confinement in present-day devices [49, 50].

VI. COMBINED IMPACT OF THE HALF-WIDTH AND AMPLITUDE OF THE LOGARITHMIC FAST ION TEMPERATURE GRADIENT

In the two preceding Sections, we have investigated the separate effect of variations in the (i) amplitude ($\omega_{T_{h,0}}$) and (ii) half-width (δ_x) of the Gaussian-like logarithmic fast ion temperature gradient on the F-ATB formation and global properties. Consistently with the quasi-linear predictions of Ref. [27, 28], we found a threshold in $\omega_{T_{h,0}}$ and in the ratio T_h/T_e to trigger the transport barrier effectively. This value corresponds to the energetic particle temperature (at fixed T_e) moving the resonant layers in the beneficial (negative) fast particle drive region (thus requiring a sufficiently large $\omega_{T_{h,0}}$ to create the beneficial drive region). When this condition is fulfilled, fast particles deplete the turbulent energy content, leading to a localized transport reduction and, hence, to the F-ATB formation. For a fixed value of the amplitude of the Gaussian-like fast particle profiles, on the other hand, δ_x is found to influence the radial extent of the transport barrier. In particular, it affects the size of the radial domain reaching the "optimal" ratio of T_h/T_e (i.e., $T_h/T_e \sim [5 - 25]$ see Fig. 13a) with large logarithmic gradients.

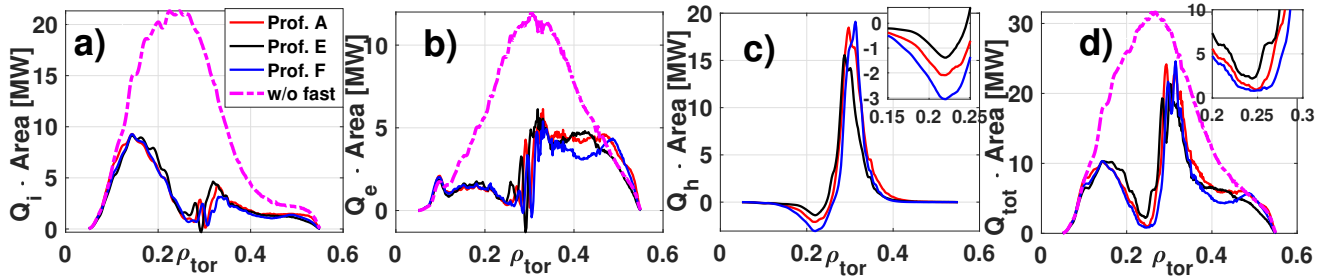In the present Section, the combined effect of $\omega_{T_{h,0}}$ and

FIG. 11. Radial profile of the a) bulk ions, b) electrons, c) hydrogen minority species and d) overall (thermal ion + electron + fast hydrogen) heat fluxes averaged over the time domain $t[c_s/a] = [400 - 600]$ corresponding to the three different fast ion profiles of Fig. 10. The inlays in c) and d) contain, respectively, a zoom into the energetic particle and total fluxes in $\rho_{tor} = [0.15 - 0.25]$ and $\rho_{tor} = [0.2 - 0.3]$. The turbulent fluxes obtained by neglecting the energetic particles (Fig. 4) are shown in magenta as reference.
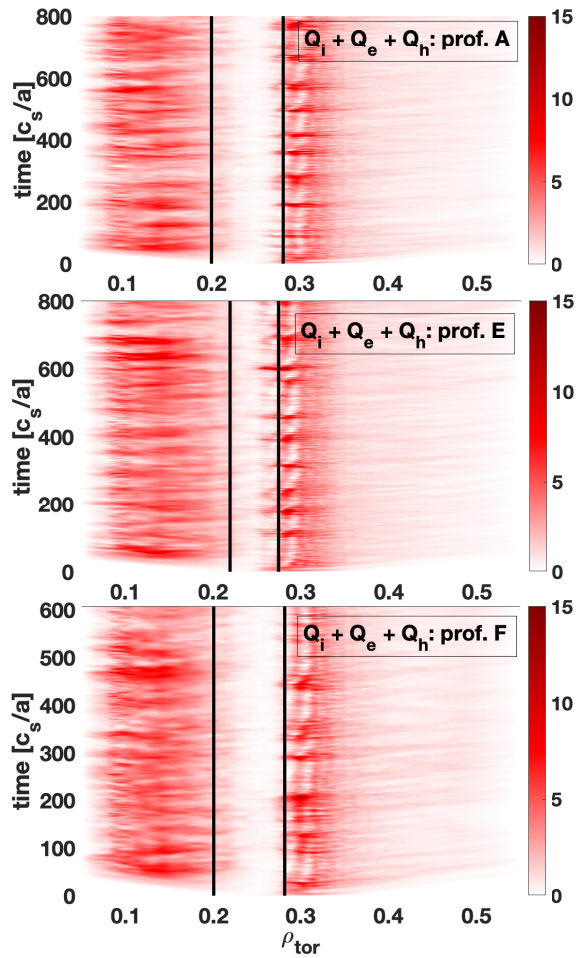
FIG. 12. Time evolution of the radial profile of the total heat flux (thermal ions + electrons + hydrogen) in MW corresponding to the cases labelled a) prof. L, b) prof. A and b) prof. I. The vertical black lines delimit the boundary positions of the transport barrier. Their radial coordinates have been computed as the position where the overall time-averaged (thermal ions + electrons + hydrogen) fluxes (see Fig. 11d) reach half-value before and after the transport barrier.
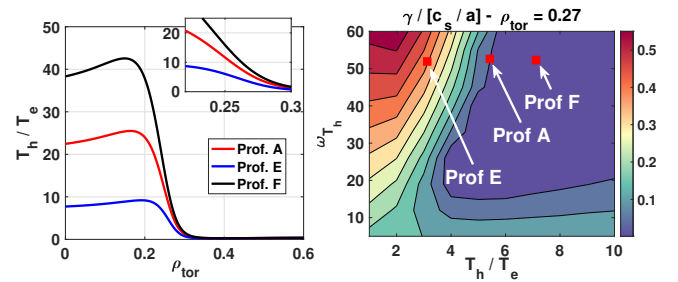

FIG. 13. a) Radial profile of the fast ion to electron temperature ratio T_h/T_e for the three different energetic particle temperature profiles of Fig. 10; and b) contour plot of the most unstable linear growth rate at the toroidal mode number $n = 21$ at $\rho_{tor} = 0.27$ for different T_h/T_e and ω_{T_h}. The reference points corresponding to the values of $(T_h/T_e, \omega_{T_h})$ for the fast ion profiles labelled prof. A, prof. E and prof. F are highlighted with red squares.
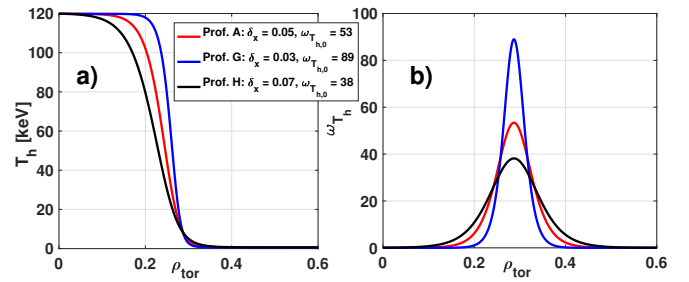

FIG. 14. Radial profiles of the hydrogen minority a) temperature and b) logarithmic temperature gradient corresponding to three different combinations of $\omega_{T_{h,0}}$ and δ_x.

δ_x is analyzed. The energetic particle profiles selected for these studies are illustrated in Fig. 14. The values of $\omega_{T_{h,0}}$ and δ_x are varied simultaneously such that the same fast ion temperature on axis is obtained. By looking at the fast ion profiles depicted in Fig. 14, we notice that - by construction - each of them reach the optimal fast

ion temperature corresponding to the "sweet-spot" observed in Fig. 8b. This is the value of T_h/T_e maximizing the stabilizing effect of the wave-particle resonant mechanism on ITG micro-instabilities. The critical difference among the radial profiles of Fig. 14a, is the radial extent of the domain where this optimal range of fast ion temperatures is located. A broader, and hence, more effective ITG stabilization is expected for the supra-thermal ion profile labeled prof. H, which is characterized by the largest δ_x. Therefore, for this specific case, the beneficial wave-particle interaction is expected to be effective in the whole region $\rho_{tor} \sim [0.2 - 0.3]$. This domain is reduced for the case labeled prof. G, defined by a smaller value of δ_x. These predictions are confirmed by the global gyrokinetic GENE results. The time-averaged radial profiles of the turbulent fluxes are shown in Fig. 15 for each different plasma species. The fast particle profile labeled prof. H leads to the most effective heat flux stabilization for the bulk species (thermal ions and electrons), whilst larger fluxes are observed for prof. G. At the radial position $\rho_{tor} = 0.2$, we notice a turbulence reduction of $\sim 50\%$ for the main ions (from $Q_i = 8.3$MW for prof. G to $Q_i = 4.4$MW for prof. H) and $\sim 50\%$ for the electrons (from $Q_e = 2.1$MW for prof. G to $Q_e = 1$MW for prof. H). The energetic particle heat flux profiles reveal a broader radial region where the fast ion heat flux is negative (inward) for prof. H, which is consistent with our previous findings of Section V. This is a signature that the wave-particle interaction is stabilizing ITG turbulence.

It is worth mentioning that despite prof. G leads to more localized transport barriers, the reduced half-width of its logarithmic temperature profile leads to a more narrow region where the wave-particle interaction is destabilizing ITGs (namely $\rho_{tor} > 0.3$). This is shown in Fig. 15c, where the radial domain of positive fast ion heat flux increases from $\rho_{tor} = [0.28 - 0.31]$ for prof. G to $\rho_{tor} = [0.27 - 0.34]$ for prof. H. However, as shown in Section IV, this outward energetic particle heat flux is strongly reduced when electromagnetic fluctuations are consistently included in the simulations.

The time evolution of the radial profile of the overall (thermal ions + electrons + fast ions) turbulent fluxes are shown in Fig. 16. This figure clearly reveals that the radial extent of the transport barrier increases by roughly 65% (from $\Delta_x = 0.055$ to $\Delta_x = 0.092$) when replacing the fast particle profile prof. G with prof. H, possibly leading to better plasma performances in experiments.

These results are again consistent with linear flux-tube results. They are shown in Fig. 17b for the toroidal mode number $n = 21$ at the radial position $\rho_{tor} = 0.22$. In particular, we notice that the strongest fast particle stabilization is observed for the case labelled prof. H and it is progressively reduced for prof. A and prof. G. The latter case exhibits large values for the ratio T_h/T_e and small logarithmic gradients. Therefore, the beneficial wave-particle resonant stabilization is weakened when compared to the other fast particle profiles (being it enhanced

by ω_{T_h}), thus leading to a reduction in the radial extend of the transport barrier. The radial profile of the ratio T_h/T_e for the differences cases studied in this Section is illustrated in Fig. 17a.

VII. RELEVANCE OF THE POSITION OF THE ICRH HEATING

The remaining free parameter defining the energetic particle temperature and its gradient is ρ_0. It determines the radial location of the peak of the logarithmic fast ion temperature gradient and, hence, it affects the position of the F-ATB. For these studies, the global gyrokinetic results of the reference profile (prof. A, i.e. $\rho_0 = 0.287$) are compared with those obtained by moving it by $\Delta\rho_0 = 0.05$ towards the magnetic axis (prof. L, i.e. $\rho_0 = 0.237$) or the edge (prof. I, i.e. $\rho_0 = 0.337$). These profiles are illustrated in Fig. 18. The amplitude and the half-width of the fast ion temperature gradients are kept constant. Although this is only a rough approximation that hardly reflects the experimental conditions, this Section aims to disentangle the impact of ρ_0 on the transport barrier from the other terms defining its radial shape (see Eq. 1).

The time-averaged heat fluxes obtained with these fast particle profiles are shown in Fig. 19 for each different plasma species. It is worth mentioning that modifications on the radially dependent block-structured velocity grids were required to resolve the velocity directions correctly. This also led to the extension of the radial grid for the case labeled prof. I, covering up to $\rho_{tor} = 0.65$. The other grids end at $\rho_{tor} = 0.55$. A first interesting observation by looking at Fig. 19 is that the extension of the radial domain for the case prof. I does not lead to significant changes in the turbulent fluxes for $\rho_{tor} > 0.4$ for the cases prof. A and I, suggesting a negligible impact of the buffer zones on the results presented within this paper. Furthermore, we notice that the (bulk + fast) ion and electron heat fluxes are strongly affected by the changes in the energetic particle profiles. More precisely, the central region of minimum turbulent transport marking the location of the F-ATB ($\bar{\rho}_0$) follows the position of the peak of the energetic particle temperature gradient. It is $\bar{\rho}_0 \sim 0.25$ for the case labeled prof. A, whilst it moves to $\bar{\rho}_0 \sim 0.2$ for prof. L, and to $\bar{\rho}_0 \sim 0.28$ for prof. I. It is worth mentioning here that the center of the F-ATB does not coincide with the position of the maximum of the fast ion logarithmic Gaussian-like temperature gradient, but it is rather determined by the ratio T_h/T_e. This result is again consistent with the quasilinear predictions of Refs. [27, 28]. The "optimal" ratio T_h/T_e (and large temperature gradient) maximizing the beneficial wave-particle resonant ITG stabilization (i.e., $T_h/T_e \sim [5-25]$) locates exactly in the region of reduced transport in Fig. 20. Similarly to the results obtained for the thermal species, also the energetic particle heat flux profiles undergoes strong modifications, which are in agreement with the changes in the resonant velocity
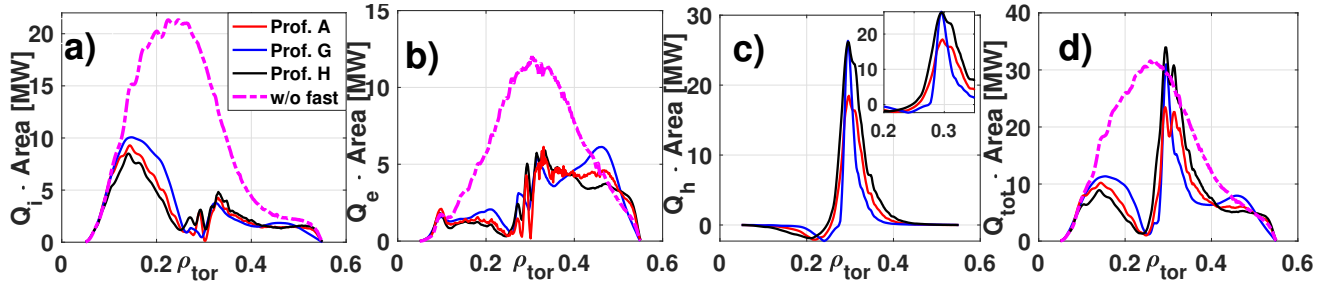
FIG. 15. Radial profile of the a) bulk ions, b) electrons, c) hydrogen minority species and d) overall (thermal ion + electron + fast hydrogen) heat fluxes averaged over the time domain $t[c_s/a] = [400 - 600]$ corresponding to the three different fast ion profiles of Fig. 14. The inlay in c) contains a zoom into the total fluxes in $\rho_{tor} = [0.2 - 0.35]$. The turbulent fluxes obtained by neglecting the energetic particles (Fig. 4) are shown in magenta as reference.
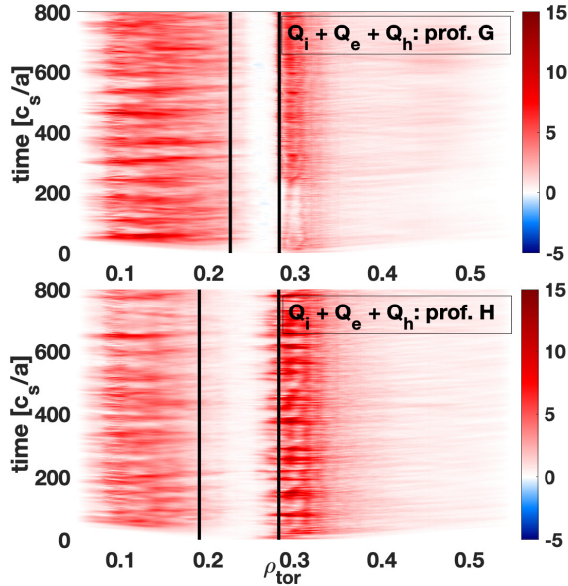

FIG. 16. Time evolution of the radial profile of the total heat flux (thermal ions + electrons + hydrogen) in MW corresponding to the cases labelled a) prof. G and b) prof. H. The vertical black lines delimit the boundary positions of the transport barrier. Their radial coordinates have been computed as the position where the overall time-averaged (thermal ions + electrons + hydrogen) fluxes (see Fig. 15d) reach half-value before and after the transport barrier.
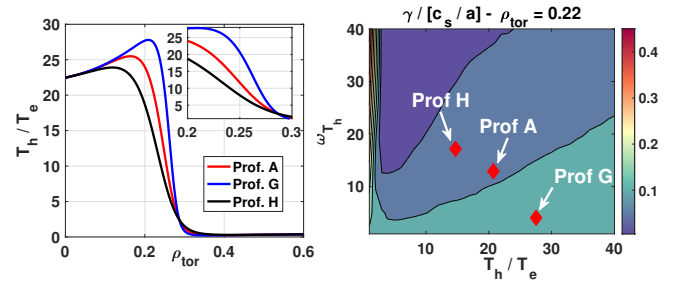

FIG. 17. a) Radial profile of the fast ion to electron temperature ratio T_h/T_e for the three different energetic particle temperature profiles of Fig. 14; and b) contour plot of the most unstable linear growth rate at the toroidal mode number $n = 21$ at $\rho_{tor} = 0.22$ for different T_h/T_e and ω_{T_h}. The reference points corresponding to the values of $(T_h/T_e, \omega_{T_h})$ for the fast ion profiles labelled prof. A, prof. G and prof. H are highlighted with red diamonds.
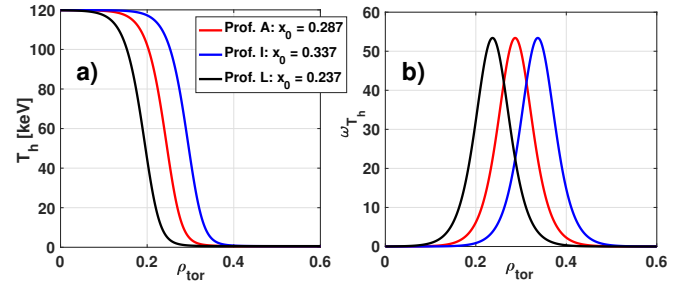

FIG. 18. Radial profiles of the hydrogen minority a) temperature and b) logarithmic temperature gradient corresponding to three different values of ρ_0.

layers, as discussed in detail in the previous Sections. The transport barrier radial dependence with the fast ion temperature profiles further corroborates the theoretical interpretation that the barrier is triggered by a wave-particle resonant interaction between supra-thermal particles and ITGs.

The time evolution of the overall turbulence fluxes are shown in Fig. 20 for the different fast particle temperature profiles. The most effective (thermal ion + electron + fast particle) turbulence stabilization is found for prof. L, where the thermal ion and electron fluxes are

strongly reduced in the region $\rho_{tor} = [0.17 - 0.245]$. For this case, the position of the transport barrier leads to a suppression of the ion and electron heat fluxes, as shown in Fig. 19a-b. On the other hand, the case labeled prof. I, moves the F-ATB outward, thus reducing its beneficial effect in the radial domain $\rho_{tor} = [0.1 - 0.25]$ that un-
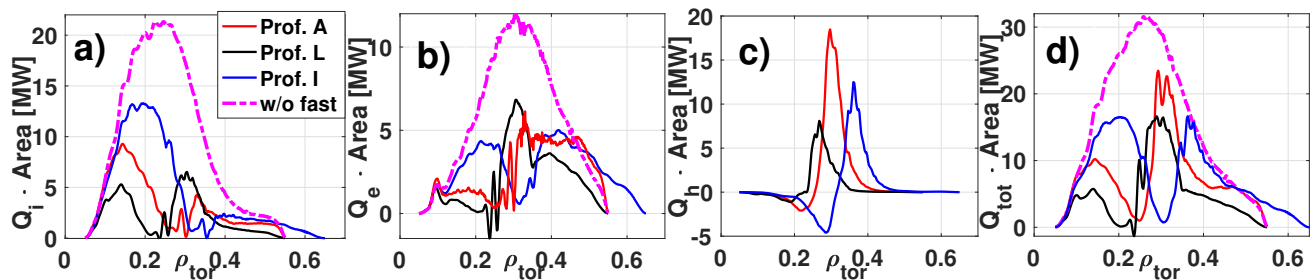
FIG. 19. Radial profile of the a) bulk ions, b) electrons, c) hydrogen minority species and d) overall (thermal ion + electron + fast hydrogen) heat fluxes averaged over the time domain $t[c_s/a] = [400 - 600]$ corresponding to the three different fast ion profiles of Fig. 18. The turbulent fluxes obtained by neglecting the energetic particles (Fig. 4) are shown in magenta as reference.

dergoes a large increase in both thermal ion and electron fluxes. These findings do not suggest that the "optimal" turbulence suppression is expected for transport barriers located more in the inner radii, but is a rather consequence of the specific numerical setup employed throughout this paper. More specifically, it depends on the particular radial profile of the bulk ion turbulent heat flux, which peaks around $\rho_{tor} \sim 0.2$ in the absence of fast ions. Therefore, the most effective turbulence suppression is found for the transport barriers centered at this location.

VIII. IMPACT OF THE $q = 1$ RATIONAL SURFACE

A large number of ITBs observed in experiments has been associated with rational surfaces in the safety factor profile triggered via fundamentally different mechanisms compared to the wave-particle interaction. In this regard, the interest towards transport barriers generated near the $q = 1$ and $q = 2$ rational surfaces has grown in recent years. The physics behind these transport barriers generation is still not fully understood. The leading explanation was proposed in Ref. [51], suggesting that fishbones or MHD activity - excited at the rational surfaces - lead to a radial resonant-fast-ion redistribution, thus generating a radial electric field which - in turn - would suppress micro-turbulence. While the excitation of a radial electric field via fast ion redistribution has been observed in MHD simulations [52, 53] (hence without turbulence), a high-fidelity simulation retaining self-consistently turbulence and fishbones - to our knowledge - has not been performed yet. Therefore, whether the amplitude of the radial electric field generated via fishbone activity would be sufficient to suppress turbulent transport and, hence, lead to a transport barrier is still a meaningful open question. This is particularly relevant since gyrokinetic simulations have shown that MHD activity - driven from energetic particles - is often leading to an increase in turbulent transport [50, 54]. This turbulence destabilization could make the impact of a radial

electric field generated via fast particle redistribution a negligible effect. From the experimental side, opposite results have been presented for different devices. While LH-2A [55] and JET [18] measure fishbone instabilities also after the onset of the ITB formation (hence they can hardly play a role in triggering the ITB), the contrary is observed at EAST [53] and ASDEX Upgrade [18].

In the remaining section we analyze the possible impact of the $q = 1$ rational surface on the F-ATB. More specifically, we compare the GENE results of Fig. 9 - performed on the safety factor profile reconstructed via CLISTE (with no $q = 1$ rational surface) - with the ones obtained on a different safety factor profile containing the $q = 1$ rational surface at $\rho_{tor} = 0.36$. This safety factor profile has been reconstructed with IDE on the reference ASDEX Upgrade discharge #36637 at $t = 4.1s$. The two safety factor profiles are illustrated in Fig. 22.

The time-averaged heat fluxes obtained with the CLISTE and IDE safety factor profiles are shown in Fig. 23 for each different plasma species. We note that the radial resolution of the GENE simulations was increased to $nx0 = 512$ to resolve the spatial scales close to the rational surface. Moreover, the minimum toroidal mode number was reduced from $n_{min} = 2$ to $n_{min} = 1$ with a corresponding increase in the bi-normal resolution from $nky0 = 32$ to $nky0 = 64$ to retain the $n = 1$ fishbone excited at the rational surface $q = 1$ and cover the same spectra than the one studied in our previous GENE analyses. The energetic particle equilibrium distribution function has been modeled with a bi-Maxwellian distribution function and the parallel and perpendicular temperature profiles have been set equal to the ones computed by TORIC/SSFPQL (as previously done in Sec. IV). These changes in the numerical setup led to a significant increase in the computing time of these simulations, each requiring approximately 1.5 million CPU·h on the Marconi Skylake partition. By looking at the electrostatic results of Fig. 23 we note that the modifications in the safety factor profiles lead to a reduction in the thermal turbulent fluxes in the whole radial region of interest. When we retain electromagnetic fluctuations ($\beta_e(\rho_{tor} = 0.3) = 0.35\%$), no qualitative difference is ob-
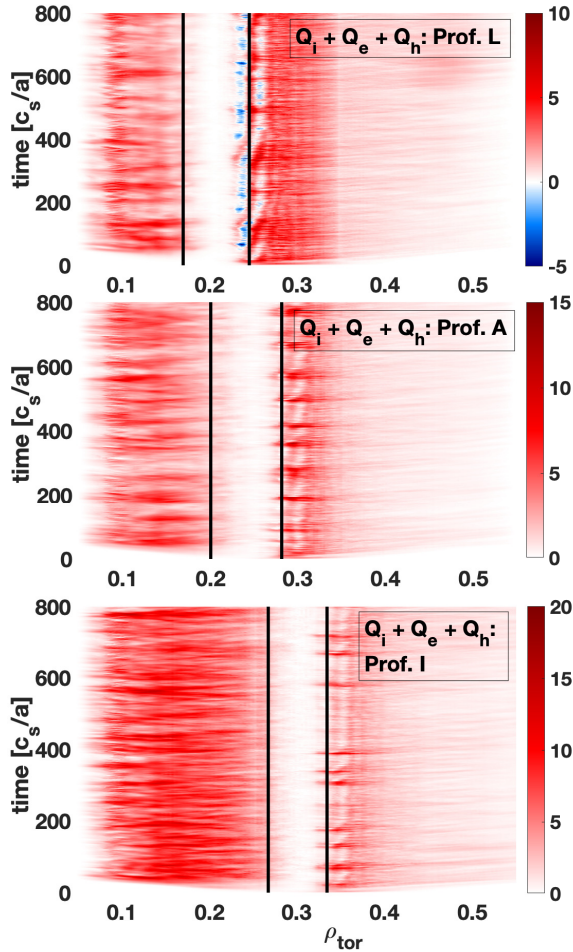
FIG. 20. Time evolution of the radial profile of the total heat flux (thermal ions + electrons + hydrogen) in MW corresponding to the cases labelled a) prof. L, b) prof. A and b) prof. I. To compare more easily the changes in the position of the F-ATB among the different profiles, the radial domain of the case labelled prof. I has been set equal to $\rho_{tor} = [0.05 - 0.55]$. The vertical black lines delimit the boundary positions of the transport barrier. Their radial coordinates have been computed as the position where the overall time-averaged (thermal ions + electrons + hydrogen) fluxes (see Fig. 19d) reach half-value before and after the transport barrier.
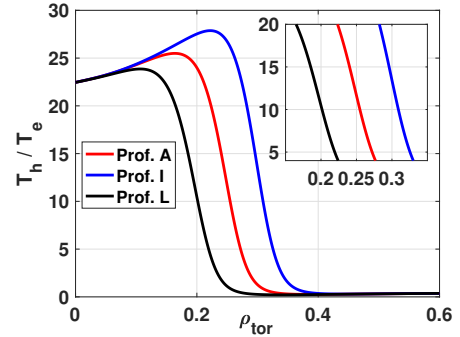

FIG. 21. Radial profile of the fast ion to electron temperature ratio T_h/T_e for the three different energetic particle temperature profiles of Fig. 18.
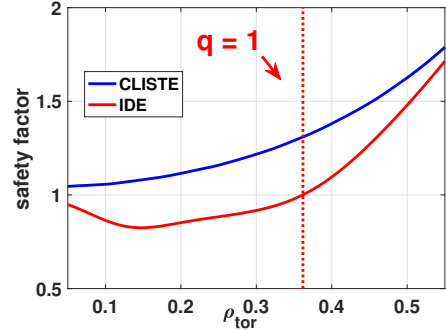

FIG. 22. Comparison of the safety factor profile reconstructed by CLISTE (blue line) with the one computed via IDE (red line) for the ASDEX Upgrade discharge #36637 at $t = 4.1$s. IDE predicts a rational surface $q = 1$ at $\rho_{tor} = 0.36$, marked by the vertical dotted line.

served on the turbulent fluxes between the CLISTE and IDE setups, except for the additional stabilization found in the electrostatic GENE simulation for the IDE safety factor. This additional stabilization is consistent with the ITG dependence with the safety factor [56], which predicts a larger ITG critical gradient as q is reduced. Interestingly, we notice a minor increase of the electron heat flux in the electromagnetic simulation with respect to the electrostatic one. These preliminary results suggest that the presence of the $q = 1$ rational surface does not impact the F-ATB properties, and no enhancement of turbulent stabilization is observed at the proximity of the

barrier. Further studies will be performed in the near future to evaluate the possible interplay between fishbones and ITBs also on different plasma conditions where fishbones are considered the transport barrier trigger mechanism.

IX. CONCLUSIONS

A series of global nonlinear GENE simulations has been performed to investigate the impact of (i) different energetic particle temperature profiles and (ii) the presence of the rational surface $q = 1$ on a novel type of transport barrier called F-ATB. More specifically, we have analyzed how the particular shape of the suprathermal ion temperature (and corresponding logarithmic gradient) determines the transport barrier width, radial localization, and its impact on turbulent transport and, finally, how the presence of the $q = 1$ rational surface affects the F-ATB generation.

Realistic ASDEX Upgrade physical parameters - inspired from the discharge #36637 at $t = 4.1$s - have
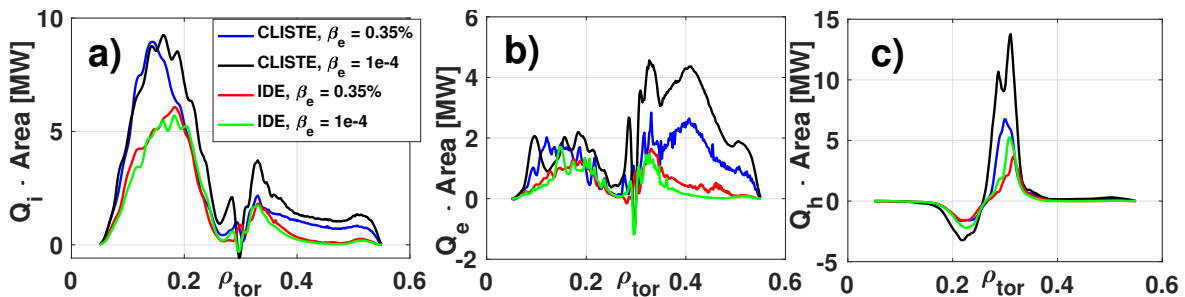
FIG. 23. Radial profile of the heat flux of a) bulk ions, b) electrons and c) hydrogen minority species - averaged over the time domain $t[c_s/a] = [400 - 600]$ corresponding to the fast particle profile labelled prof. A and different values of $\beta_e(\rho_{tor} = 0.3)$.

been considered, and an analytic approximation for the fast ion temperature has been used. This is defined by a Gaussian-like logarithmic temperature gradient with essentially three free parameters, namely the amplitude $(\omega_{T_{h,0}})$, the half-width (δ_x) and the radial location (ρ_0) of the Gaussian-like peak. Corresponding nonlinear scans over these different parameters are performed. Moreover, the role of finite β_e (electromagnetic) effects and energetic particle temperature anisotropies - arising, e.g., from the heating schemes - on the transport barrier has been studied. It is worth mentioning that despite the relevance of the supra-thermal ion density in the dynamics of the wave-particle resonant interaction, for simplicity, it has been fixed to the value $n_h/n_e = 0.11\%$. This is the nominal fast ion density measured in the ASDEX Upgrade discharge #36637 at $t = 4.1$s inferred from neutral-particle-analyzer measurements. This holds true for the entire radial domain considered for the GENE simulations, thus fixing also the fast hydrogen logarithmic density gradient profile, which has not been varied throughout this work.

The majority of the GENE simulations have been performed with a safety factor profile reconstructed by CLISTE [38] on the ASDEX Upgrade discharge #36637 at $t = 4.1$s, which predicts a monotonic safety factor profile always above $q = 1$. However, the safety factor computed via IDE on the same time-slice of this discharge presents a rational surface $q = 1$ at $\rho_{tor} = 0.36$. The possible impact of this rational surface on the transport barrier properties has been analyzed with radially global GENE electromagnetic simulations.

The main findings can be summarized as follows:

(i) We found a threshold in the amplitude of the logarithmic temperature gradient $\omega_{T_{h,0}}$ and in the ratio of T_h/T_e to trigger the transport barrier. This is related to the minimum value of $\omega_{T_{h,0}}$ required for the fast ion temperature profile to increase up to the "optimal" range of temperatures where $T_h/T_e = [5 - 25]$. When this condition is fulfilled, the magnetic fast particle drift matches the linear ITG frequencies (for the non-linearly relevant wave-numbers) in the negative fast ion drive regions $(v_\parallel^2 + \mu B_0 < 3/2)$, thus strongly suppressing the

ITG drive. This leads to a localized (only in the radial domain where such conditions are fulfilled) turbulence reduction. It is important to mention here that the threshold value is also expected to depend on the local (at the position of interest) fast ion density. A smaller fast ion density will require a larger logarithmic fast ion temperature gradient to maximize the wave-particle resonant interaction. According to Refs. [27, 28] the flow of the overall resonant energy exchange is proportional to both the fast ion density and its logarithmic temperature gradient.

(ii) The half-width δ_x of the Gaussian-like logarithmic fast particle temperature profile controls the radial width of the transport barrier. More specifically, it affects the size of the radial domain reaching the "optimal" ratio of T_h/T_e (i.e., $T_h/T_e \sim [5 - 25]$). Therefore, for a fixed value of $\omega_{T_{h,0}}$, the largest value of δ_x is found to lead to the widest transport barrier. In particular, by assuming that the relation $\omega_{T_h} \gg \omega_{n_h}$ is always fulfilled, different fast particle profiles (starting all with the same boundary value at the plasma edge) can reach the optimal value of T_h/T_e only if the fast ion logarithmic temperature gradient is sufficiently large to let the fast ion profile increase from being almost "thermal" to values having $T_h/T_e = [5 - 25]$. For this reason, to reach these fast ion temperatures we have an effective threshold to be overcome in the logarithmic fast ion temperature gradient $\omega_{T,h}$. In this paper $\omega_{T,h}$ is defined (for a fixed ρ_0) by two parameters, namely $\omega_{T_{h,0}}$ and δ_x (see Eq. 2). When δ_x is fixed, the threshold to overcome in $\omega_{T_{h,0}}$ to reach the optimal values of T_h/T_e is solely determined by $\omega_{T_{h,0}}$ and for the case studied in Sec.IV it corresponds to $\omega_{T_{h,0}} = 42$. However, when the value of δ_x is increased in Sec.VI the threshold in $\omega_{T_0,c}$ is reduced down to the value $\omega_{T_0,c} = 38$.

(iii) When the on-axis fast ion temperature is fixed, the "optimal" profile has the largest half-width (despite the consequent reduction in $\omega_{T_{h,0}}$), since fixing it leads to fast ion temperature profiles always

reaching the "sweet-spot" in T_h/T_e. This enhances the wave-particle resonant interaction. Therefore, all these profiles can efficiently trigger the F-ATB. However, the one with the largest half-width will lead to the broader transport barrier, thus amplifying its effect on transport.

(iv) The central position of the transport barrier is "mainly" controlled by ρ_0 (position of the maximum of the Gaussian-like peak in the fast ion logarithmic temperature profile). Here, we are considering that the electron temperature profile does not vary dramatically along the radial direction. This will otherwise affect the ratio T_h/T_e. For the bulk profiles employed throughout this paper, the most effective overall turbulence suppression is found when the position of the peak is moved in the inner radii. This is strictly linked to the radial profile of the thermal ion turbulent flux in the absence of fast particles, which peaks around $\rho_{tor} \sim 0.2$. This result can change in other physical conditions where the bulk ion ITG turbulence is localized at a different position.

(v) Electromagnetic fluctuations do not alter qualitatively the transport barrier properties. However, finite β_e effects lead to additional turbulence stabilization mainly in the radial region where the fast particle temperature gradient is maximum. No linearly unstable Alfvénic fast-ion driven modes are observed. These findings are in agreement with the results of Ref. [45, 46] where a nonlinear interplay between marginally stable fast ion modes and turbulence has been proposed to explain the electromagnetic fast particle turbulence stabilization [44].

(vi) Velocity space anisotropies do not lead to significant modifications on the thermal species fluxes in the electrostatic GENE results. However, non negligible changes are observed for the supra-thermal particles. This is likely to be related to the corresponding variations in the fast ion drive term (namely $\partial_x F_{0,h}$) which in turn affect the free-energy exchange between fast ions and ITG turbulence.

(vii) The rational surface $q = 1$ on the safety factor profile does not affect the F-ATB properties and no additional turbulence suppression (related to the presence of the rational surface) is observed in the electromagnetic GENE simulations containing the $q = 1$ surface. However, given the present limitations of our codes, we cannot exclude (based only on the results of Section VIII) that rational surfaces play a role in triggering and sustaining the transport barrier in the ASDEX Upgrade discharge #36637, as suggested e.g. in Ref. [18, 51].

The impact of such findings on plasma profiles evolution and plasma performances is still unclear. In particular, being able to predict with numerical simulations what are the critical energetic particle density, heating power and location of the ICRH absorption layer to trigger the most effective transport barrier is extremely challenging considering the numerical tools available to date. The previously mentioned quantities (energetic particle density, heating power and location of the ICRH absorption layer) depend on each others in a way which cannot be captured by gradient-driven turbulence simulations. These analyses would require the plasma profiles to freely evolve due to the combined effect of external sources and turbulent fluxes and hence a flux-driven (electromagnetic) approach, which is still not affordable numerically. An attractive alternative to flux-driven simulations is coupling the gradient-driven GENE version (acting on the short turbulence time scale) with a transport code (acting on the transport time scale). Dedicated studies pursuing this method are currently ongoing [57] and will be extended to include kinetic electrons and suprathermal particles in the near future.

Appendix A: Convergence studies

To ensure that the transport barrier formation is not an artifact of the particular numerical setup employed, convergence studies have been performed and are illustrated throughout this Section. In particular, we analyze in details convergence over the radial and velocity (both $v_{\parallel}$ and μ) resolutions together with different choices for the radially dependent block-structured velocity grid. The numerical setup and physical parameters are the same as the ones summarized in Section II. Given the prohibitive computational cost for performing such studies for each of the ten different fast particle profiles employed in this manuscript, we limit our analyses only to the reference profile labelled prof. A.

1. Radial resolution

The number of radial grid points (nx0) employed throughout this work is nx0 = 256. This resolution differs from the one used in Ref. [26] (namely nx0 = 512) by a factor of two to reduce the otherwise prohibitive computational cost required to run the ten different global simulations performed here. A comparison of the time-averaged radial profile of the heat fluxes carried by

each of the plasma species is illustrated in Fig. 24 for nx0 = 128, nx0 = 256 and nx0 = 512. The radial domain mid-radius location is $\rho_{tor} = 0.3$. It corresponds to the reference position used to normalize the different physical parameters. At this location, $1/\rho^* = a/\rho_s = 176$, with a minor radius of the devise, $\rho_s = c_s/\Omega_i$, $c_s = (T_e/m_e)^{1/2}$. Therefore, the expected minimum radial resolution required to correctly resolve the radial dynamics is roughly two point per thermal ion Larmor radius. However, Fig. 24 reveals only minor differences in the heat fluxes when increasing nx0 from 256 to 512. This result shows that a minimum radial resolution of nx0 = 256 is sufficient to ensure converged heat fluxes for each plasma species within < 7% error. This relatively small minimum radial resolution may be due to the absence of low m/n rational surfaces in the radial domain of interest.

2. Velocity resolution

The F-ATB trigger mechanism is the wave-particle resonant interaction discussed in Ref. [27, 28]. This is a complex effect involving a phase-space resonance in the velocity space. Therefore, it is particularly important to correctly resolve the $(v_\parallel, \mu)$ directions and ensure that the resonant layers are well captured. In the present Section, convergence studies are performed comparing the time-averaged radial heat flux profiles obtained with the reference velocity resolution employed in Sections (i.e., $(nv0, nw0) = (48, 24)$), and $(nv0, nw0) = (96, 48)$. The results are illustrated in Fig. 25 for the different plasma species considered. The increase by a factor of two in the parallel velocity and magnetic moment resolutions leads to $\sim 12\%$ variations in the radially-averaged turbulent fluxes, proving that the reference results are reasonably well resolved in the velocity directions.

3. Block-structured grid

The remaining convergence study discussed within this paper concerns the particular shape of the radially dependent block-structured grid employed for the global GENE simulations. As already stressed in Section II, this particular feature is essential to reduce the velocity resolution requirements to resolve the dynamics of the bulk and supra-thermal species in the whole radial domain of interest. Therefore, to ensure that our numerical results are not affected by the specific choice of the block-structured grid, we present a comparison of the time-averaged turbulent fluxes obtained with the reference grid (see Fig. 1) and with the one introduced in Fig. 26. The results are shown in Fig. 27 for the different plasma species considered. The same grid resolution is employed in each directions with $(nv0, nw0) = (96, 48)$. The change in the radially-dependent velocity grid does not alter the numerical results significantly and only minor differences of about $\sim 10\%$ are observed from Fig. 27. These findings show that the reference results are independent from the particular choice of the block-structured grid and well resolved in the radial and velocity directions.

[1] J. Connor, T. Fukuda, X. Garbet, C. Gormezano, V. Mukhovatov, M. Wakatani, the ITB Database Group, the ITPA Topical Group on Transport, and I. B. Physics, Nuclear Fusion 44, R1 (2004).

[2] B. W. Rice, K. H. Burrell, L. L. Lao, G. Navratil, B. W. Stallard, E. J. Strait, T. S. Taylor, M. E. Austin, T. A. Casper, M. S. Chu, C. B. Forest, P. Gohil, R. J. Groebner, W. W. Heidbrink, A. W. Hyatt, H. Ikezi, R. J. La Haye, E. A. Lazarus, Y. R. Lin-Liu, M. E. Mauel, W. H. Meyer, C. L. Rettig, D. P. Schissel, H. E. St. John, P. L. Taylor, and A. D. Turnbull, Physics of Plasmas 3, 1983 (1996).

[3] O. Gruber, R. Wolf, R. Dux, S. Guenter, P. J. M. Carthy, K. Lackner, M. Maraschek, H. Meister, G. Pereverzev, W. Treutterer, and the ASDEX Upgrade Team, Plasma Physics and Controlled Fusion 42, A117 (2000).

[4] G. Tardini, J. Hobirk, V. Igochine, C. Maggi, P. Martin, D. McCune, A. Peeters, A. Sips, A. Stäbler, J. Stober, and the ASDEX Upgrade Team, Nuclear Fusion 47, 280 (2007).

[5] T. Fujita, S. Ide, H. Shirai, M. Kikuchi, O. Naito, Y. Koide, S. Takeji, H. Kubo, and S. Ishida, Phys. Rev. Lett. 78, 2377 (1997).

[6] F. M. Levinton, M. C. Zarnstorff, S. H. Batha, M. Bell, R. E. Bell, R. V. Budny, C. Bush, Z. Chang, E. Fredrickson, A. Janos, J. Manickam, A. Ramsey, S. A. Sabbagh, G. L. Schmidt, E. J. Synakowski, and G. Taylor, Phys. Rev. Lett. 75, 4417 (1995).

[7] X. Litaudon, T. Aniel, Y. Baranov, D. Bartlett, A. Bécoulet, C. Challis, G. D. Conway, G. A. Cottrell, A. Ekedahl, M. Erba, L. Eriksson, C. Gormezano, G. T. Hoang, G. Huysmans, F. Imbeaux, E. Joffrin, M. Mantsinen, V. Parail, Y. Peysson, F. Rochard, P. Schild, A. Sips, F. X. Säöldner, B. Tubbing, I. Voitsekhovitch, D. Ward, and W. Zwingmann, Plasma Physics and Controlled Fusion 41, A733 (1999).

[8] D. R. Ernst, P. T. Bonoli, P. J. Catto, W. Dorland, C. L. Fiore, R. S. Granetz, M. Greenwald, A. E. Hubbard, M. Porkolab, M. H. Redi, J. E. Rice, K. Zhurovich, and A. C.-M. Group, Physics of Plasmas 11, 2637 (2004).

[9] K. Zhurovich, C. Fiore, D. Ernst, P. Bonoli, M. Greenwald, A. Hubbard, J. Hughes, E. Marmar, D. Mikkelsen, P. Phillips, and J. Rice, Nuclear Fusion 47, 1220 (2007).

[10] C. Gormezano, Plasma Physics and Controlled Fusion 41, B367 (1999).

[11] K. Ida, T. Shimozuma, H. Funaba, K. Narihara, S. Kubo, S. Murakami, A. Wakasa, M. Yokoyama, Y. Takeiri, K. Y. Watanabe, K. Tanaka, M. Yoshinuma, Y. Liang, and N. Ohyabu (LHD experimental group), Phys. Rev. Lett. 91, 085003 (2003).
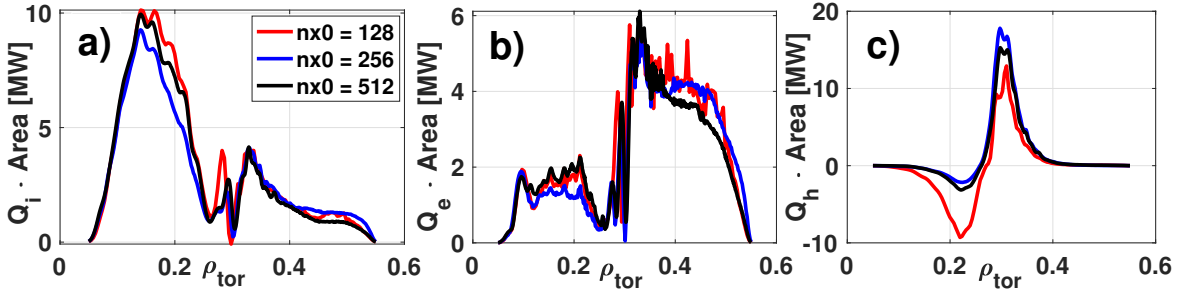
FIG. 24. Radial profile of the a) bulk ion, b) electron and c) hydrogen minority heat fluxes averaged over the time domain $t[c_s/a] = [200 - 300]$ corresponding to the reference profiles labelled prof. A for different radial grid resolutions.
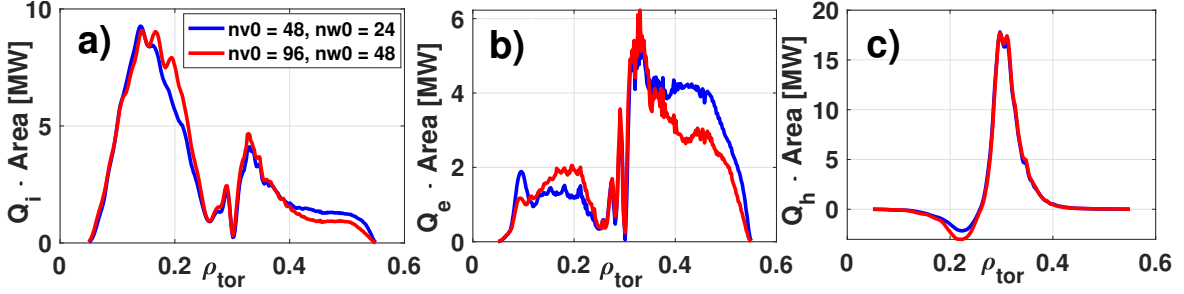

FIG. 25. Radial profile of the a) bulk ion, b) electron and c) hydrogen minority heat fluxes averaged over the time domain $t[c_s/a] = [200 - 300]$ corresponding to the reference profiles labelled prof. A for different velocity grid resolutions.
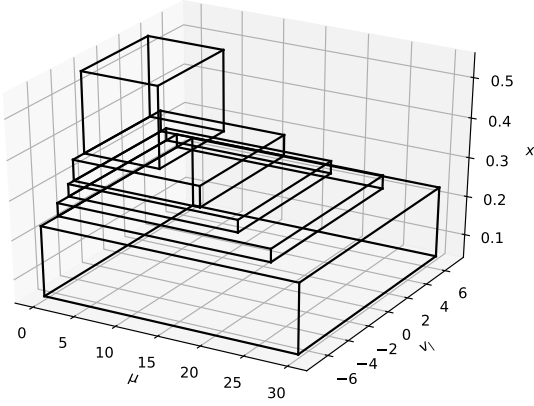

FIG. 26. Block-structured grid with five blocks in $(\rho_{tor}, v_\parallel, \mu)$ generated to check the convergence of the GENE results.

[12] A. Fujisawa, H. Iguchi, T. Minami, Y. Yoshimura, H. Sanuki, K. Itoh, S. Lee, K. Tanaka, M. Yokoyama, M. Kojima, S.-I. Itoh, S. Okamura, R. Akiyama, K. Ida, M. Isobe, S. Morita, S. Nishimura, M. Osakabe, A. Shimizu, C. Takahashi, K. Toi, Y. Hamada, K. Matsuoka, and M. Fujiwara, Phys. Rev. Lett. **82**, 2669 (1999).

[13] F. Castejón, V. Tribaldos, I. García-Cortés, E. de la Luna, J. Herranz, I. Pastor, T. Estrada, and TJ-II Team,

Nuclear Fusion **42**, 271 (2002).

[14] U. Stroth, K. Itoh, S.-I. Itoh, H. Hartfuss, H. Laqua, the ECRH team, and the W7-AS team, Phys. Rev. Lett. **86**, 5910 (2001).

[15] E. Joffrin, C. Challis, T. Hender, D. Howell, and G. Huysmans, Nuclear Fusion **42**, 235 (2002).

[16] E. Joffrin, G. Gorini, C. D. Challis, N. C. Hawkes, T. C. Hender, D. F. Howell, P. Maget, P. Mantica, D. Mazon, S. E. Sharapov, G. Tresset, and contributors to the EFDA-JET Workprogramme, Plasma Physics and Controlled Fusion **44**, 1739 (2002).

[17] X. Garbet, C. Bourdelle, G. T. Hoang, P. Maget, S. Benkadda, P. Beyer, C. Figarella, I. Voitsekovitch, O. Agullo, and N. Bian, Physics of Plasmas **8**, 2793 (2001).

[18] E. Joffrin, R. Wolf, B. Alper, Y. Baranov, C. D. Challis, M. de Baar, C. Giroud, C. W. Gowers, N. C. Hawkes, T. C. Hender, M. Marachek, D. Mazon, V. Parail, A. Peeters, K.-D. Zastrow, and contributors to the EFDA-JET Workprogramme, Plasma Physics and Controlled Fusion **44**, 1203 (2002).

[19] E. Joffrin, C. Challis, G. Conway, X. Garbet, A. Gude, S. Günter, N. Hawkes, T. Hender, D. Howell, G. Huysmans, E. Lazzaro, P. Maget, M. Marachek, A. Peeters, S. Pinches, S. Sharapov, and JET-EFDA contributors, Nuclear Fusion **43**, 1167 (2003).

[20] K. Wong, W. Heidbrink, E. Ruskov, C. Petty, C. Greenfield, R. Nazikian, and R. Budny, Nuclear Fusion **45**, 30 (2004).

[21] M. Romanelli, A. Zocco, F. Crisanti, and JET-EFDA Contributors, Plasma Physics and Controlled Fusion **52**,
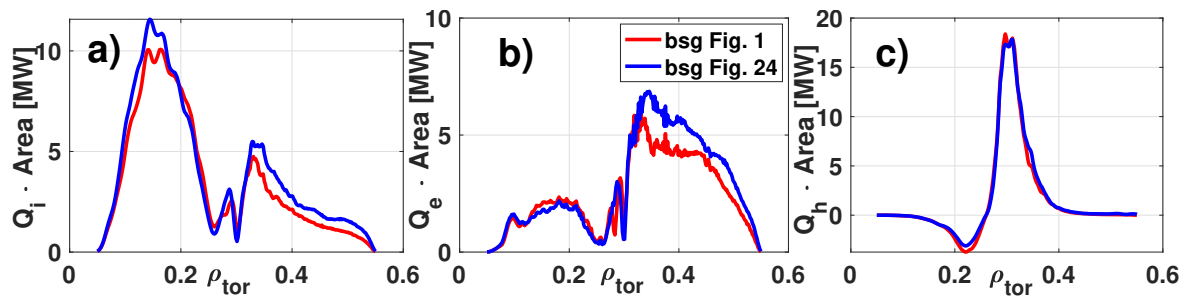
FIG. 27. Radial profile of the a) bulk ion, b) electron and c) hydrogen minority heat fluxes averaged over the time domain $t[c_s/a] = [200 - 300]$ corresponding to the reference profiles labelled prof. A for different block-structured grids.

045007 (2010).

[22] G. Dif-Pradalier, G. Hornung, P. Ghendrih, Y. Sarazin, F. Clairet, L. Vermare, P. H. Diamond, J. Abiteboul, T. Cartier-Michaud, C. Ehrlacher, D. Estève, X. Garbet, V. Grandgirard, O. D. Gürcan, P. Hennequin, Y. Kosuga, G. Latu, P. Maget, P. Morel, C. Norscini, R. Sabot, and A. Storelli, Phys. Rev. Lett. **114**, 085004 (2015).

[23] A. Strugarek, Y. Sarazin, D. Zarzoso, J. Abiteboul, A. S. Brun, T. Cartier-Michaud, G. Dif-Pradalier, X. Garbet, P. Ghendrih, V. Grandgirard, G. Latu, C. Passeron, and O. Thomine, Plasma Physics and Controlled Fusion **55**, 074013 (2013).

[24] F. Jenko, W. Dorland, M. Kotschenreuther, and B. N. Rogers, Phys. Plasmas **7**, 1904 (2000).

[25] T. Görler, X. Lapillonne, S. Brunner, T. Dannert, F. Jenko, F. Merz, and D. Told, Journal of Computational Physics **230**, 7053 (2011).

[26] A. Di Siena, R. Bilato, T. Görler, A. Bañón Navarro, E. Poli, V. Bobkov, D. Jarema, E. Fable, C. Angioni, Y. O. Kazakov, R. Ochoukov, P. Schneider, M. Weiland, F. Jenko, and the ASDEX Upgrade Team, Phys. Rev. Lett. **127**, 025002 (2021).

[27] A. Di Siena, T. Görler, H. Doerk, E. Poli, and R. Bilato, Nucl. Fusion **58**, 054002 (2018).

[28] A. Di Siena, T. Görler, E. Poli, R. Bilato, H. Doerk, and A. Zocco, Physics of Plasmas **26**, 052504 (2019).

[29] A. Di Siena, A. Bañón Navarro, and F. Jenko, Phys. Rev. Lett. **125**, 105002 (2020).

[30] N. Bonanomi, P. Mantica, A. D. Siena, E. Delabie, C. Giroud, T. Johnson, E. Lerche, S. Menmuir, M. Tsalas, and D. V. E. and, Nuclear Fusion **58**, 056025 (2018).

[31] A. Di Siena, T. Görler, H. Doerk, J. Citrin, T. Johnson, M. Schneider, E. Poli, and JET Contributors, J. Phys. Conf. Ser. **775**, 012003 (2016).

[32] A. Di Siena, T. Görler, H. Doerk, R. Bilato, J. Citrin, T. Johnson, M. Schneider, E. Poli, and JET Contributors, Physics of Plasmas **25**, 042304 (2018).

[33] A. D. Siena, A. Biancalani, T. Görler, H. Doerk, I. Novikau, P. Lauber, A. Bottino, E. Poli, and The ASDEX Upgrade Team, Nuclear Fusion **58**, 106014 (2018).

[34] P. Crandall, D. Jarema, H. Doerk, Q. Pan, G. Merlo, T. Görler, A. Bañón Navarro, D. Told, M. Maurer, and F. Jenko, Computer Physics Communications , 107360 (2020).

[35] D. Jarema, H. Bungartz, T. Görler, F. Jenko, T. Neckel, and D. Told, Computer Physics Communications **198**,

[36] T. Görler, X. Lapillonne, S. Brunner, T. Dannert, F. Jenko, S. K. Aghdam, P. Marcus, B. F. McMillan, F. Merz, O. Sauter, D. Told, and L. Villard, Physics of Plasmas **18**, 056103 (2011).

[37] A. Di Siena, R. Bilato, T. Görler, A. Bañón Navarro, E. Poli, V. Bobkov, D. Jarema, E. Fable, C. Angioni, Y. O. Kazakov, R. Ochoukov, P. Schneider, M. Weiland, F. Jenko, and the ASDEX Upgrade Team, (2021), arXiv:2010.14839v1 [physics.plasm-ph].

[38] P. J. Mc Carthy, Physics of Plasmas **6**, 3554 (1999).

[39] P. Xanthopoulos, W. A. Cooper, F. Jenko, Y. Turkin, A. Runov, and J. Geiger, Physics of Plasmas **16**, 082303 (2009).

[40] R. Fischer, L. Giannone, J. Illerhaus, P. J. McCarthy, R. M. McDermott, and A. U. Team, Fusion Science and Technology **76**, 879 (2020).

[41] R. Fischer, C. J. Fuchs, B. Kurzan, W. Suttrop, E. Wolfrum, and A. U. Team, Fusion Science and Technology **58**, 675 (2010).

[42] M. Brambilla and R. Bilato, Nucl. Fusion **49**, 085004 (2009).

[43] R. Bilato, M. Brambilla, O. Maj, L. Horton, C. Maggi, and J. Stober, Nuclear Fusion **51**, 103034 (2011).

[44] J. Citrin, F. Jenko, P. Mantica, D. Told, C. Bourdelle, J. Garcia, J. W. Haverkort, G. M. D. Hogeweij, T. Johnson, and M. J. Pueschel, Phys. Rev. Lett. **111**, 155001 (2013).

[45] A. D. Siena, T. Görler, E. Poli, A. Bañón Navarro, A. Biancalani, and F. Jenko, Nuclear Fusion **59**, 124001 (2019).

[46] A. Di Siena, T. Görler, E. Poli, A. Bañón Navarro, A. Biancalani, R. Bilato, N. Bonanomi, I. Novikau, F. Vannini, and F. Jenko, Journal of Plasma Physics **87**, 555870201 (2021).

[47] A. Di Siena, PhD thesis, ULM University, Germany (2019), 10.18725/OPARU-29528.

[48] L. Chen and F. Zonca, Rev. Mod. Phys. **88**, 015008 (2016).

[49] J. Citrin, J. Garcia, T. Görler, F. Jenko, P. Mantica, D. Told, C. Bourdelle, D. R. Hatch, G. M. D. Hogeweij, T. Johnson, M. J. Pueschel, and M. Schneider, Plasma Phys. Controlled Fusion **57**, 014032 (2015).

[50] A. Biancalani, A. Bottino, A. D. Siena, O. Gürcan, T. Hayward-Schneider, F. Jenko, P. Lauber, A. Mishchenko, P. Morel, I. Novikau, F. Vannini, L. Villard, and A. Zocco, Plasma Physics and Con-

trolled Fusion **63**, 065009 (2021).

[51] S. Günter, A. Gude, J. Hobirk, M. Maraschek, S. Saarelma, S. Schade, R. Wolf, and A. U. Team, Nuclear Fusion **41**, 1283 (2001).

[52] S. Pinches, S. Günter, and A. Peeters, 28th EPS Conference on Contr. Fusion and Plasma Phys. Funchal, 18-22 June 2001 **25A**, 57 (2001).

[53] Z. Liu, W. Ge, F. Wang, Y. Liu, Y. Yang, M. Wu, Z. Wang, X. Zhang, H. Li, J. Xie, T. Lan, W. Mao, A. Liu, C. Zhou, W. Ding, G. Zhuang, and W. L. and, Nuclear Fusion **60**, 122001 (2020).

[54] A. Ishizawa, K. Imadera, Y. Nakamura, and Y. Kishimoto, Nuclear Fusion **61**, 114002 (2021).

[55] X. X. He, L. W. Yan, D. L. Yu, W. Chen, L. M. Yu, Q. Ma, L. Liu, Y. L. Wei, X. F. He, N. Zhang, Y. G. Li, T. F. Sun, L. Nie, Z. B. Shi, W. L. Zhong, M. Xu, and X. R. Duan, Plasma Physics and Controlled Fusion **64**, 015007 (2021).

[56] F. Jenko, W. Dorland, and G. W. Hammett, Physics of Plasmas **8**, 4096 (2001).

[57] J. B. Parker, L. L. LoDestro, D. Told, G. Merlo, L. F. Ricketson, A. Campos, F. Jenko, and J. A. Hittinger, Nuclear Fusion **58**, 054004 (2018).